chemosensors

Article

Construction of Cr-MIL-101@PEDOT/MIP Composite Functionalized Glassy Carbon Electrode for PFOS Electrochemical Detection

Jingru Liang [1,†], Haiying Ming [1,†], Yijun Meng [1], Qingyun Tian [1,2,*], Baoyang Lu [3,4], Chuanyi Wang [2], Haijun Du [1] and Shuai Chen [3,4,*]

[1] School of Chemistry and Chemical Engineering, Yili Normal University, Yining 835000, China; hjdu51@163.com (H.D.)
[2] School of Engineering, Shaanxi University of Science and Technology, Xi'an 710021, China; wangchuanyi@sust.edu.cn
[3] School of Pharmacy, Jiangxi Science & Technology Normal University, Nanchang 330013, China; luby@jxstnu.edu.cn
[4] Jiangxi Provincial Key Laboratory of Flexible Electronics, Flexible Electronics Innovation Institute, Jiangxi Science & Technology Normal University, Nanchang 330013, China
* Correspondence: tianqingyun2017@163.com (Q.T.); shuaichen@jxstnu.edu.cn (S.C.)
† These authors contributed equally to this work.

Abstract

Perfluorooctanesulfonate (PFOS) is a typical persistent organic pollutant, which presents a significant risk to the ecosystem and human health. Therefore, the development of a highly sensitive and effective detection technique for PFOS has aroused wide concern. In this study, for the mesoporous metal–organic frameworks (MOFs), Cr-MIL-101 were used as the precursor. And the poly(3,4-ethylenedioxythiophene) (PEDOT) using as molecularly imprinted polymers (MIPs) was loaded on Cr-MIL-101 to form a core–shell structure. The obtained Cr-MIL-101@PEDOT/MIP composites integrate the high specific surface area of Cr-MIL-101 and the specific recognition capability of PEDOT/MIP. The glassy carbon electrode (GCE) interface modified by them can specifically adsorb PFOS through electrostatic interactions, coordination by Cr metal nodes, hydrophobic interaction, and hydrogen bonding, etc. The adsorbed PFOS molecules could block the active sites at the electrode interface, causing the current decay of the redox probe. Following the quantitative analysis of peak current decay values using the Langmuir model and the Freundlich–Langmuir model, a wide detection range (0.1–200 nM) and a low detection limit (0.025 nM) were obtained. Characterization techniques including scanning electron microscopy (SEM), transmission electron microscopy (TEM), X-ray diffraction (XRD), Brunauer–Emmett–Teller (BET), X-ray photoelectron spectroscopy (XPS), and electrochemical methods were employed to validate the fabrication of the composites. Moreover, Cr-MIL-101@PEDOT/MIP/GCE showed satisfactory stability, repeatability, and selectivity, providing an effective method for the detection of PFOS in practical samples, showing a wide prospective application.

Keywords: PFOS; PEDOT; MOFs; molecularly imprinted polymers; electrochemical sensor

check for updates

Received: 21 September 2025
Revised: 18 October 2025
Accepted: 20 October 2025
Published: 27 October 2025

Citation: Liang, J.; Ming, H.; Meng, Y.; Tian, Q.; Lu, B.; Wang, C.; Du, H.; Chen, S. Construction of Cr-MIL-101@PEDOT/MIP Composite Functionalized Glassy Carbon Electrode for PFOS Electrochemical Detection. *Chemosensors* **2025**, *13*, 378. https://doi.org/10.3390/chemosensors13110378

Copyright: © 2025 by the authors. Licensee MDPI, Basel, Switzerland. This article is an open access article distributed under the terms and conditions of the Creative Commons Attribution (CC BY) license (https://creativecommons.org/licenses/by/4.0/).

1. Introduction

PFOS ($C_8F_{17}SO_3H$) belongs to perfluorinated and polyfluoroalkyl substances (PFASs), which is a typical persistent organic pollutant in the environment. It has a fully fluorinated carbon chain, and ends with a sulfonic acid group. The former feature confers it robust

photostability, thermal stability, chemical stability, and hydrophobicity [1,2], while the latter shows hydrophilicity, which enables it to have unique physicochemical properties. Therefore, it has been widely utilized in various industrial fields over the past few decades, including textile antifouling treatments, fire-fighting foams, electroplating fog inhibitors, food packaging materials, and so on [1,2]. However, it has the characteristics of persistence, bioaccumulation, and long-distance migration in the environment, which poses a potential threat to the global ecosystem and human health [3–6]. Despite the stringent regulations imposed by the Stockholm Convention on its production and utilization [7], the environmental residues caused by historical wide application still remain. Consequently, the demand for its efficient, rapid, and convenient detection is urgently increasing.

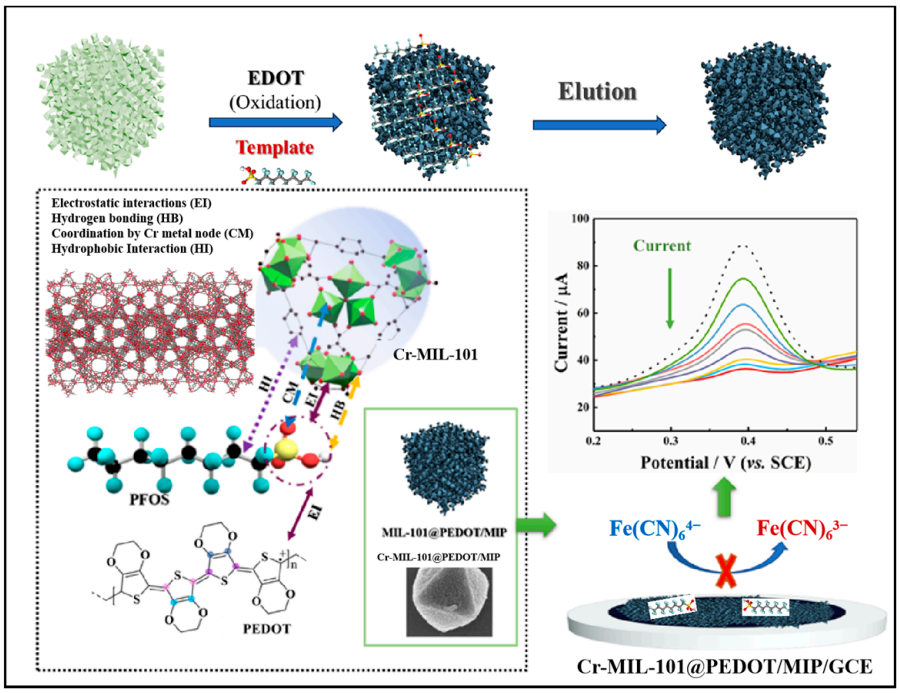
Until now, numerous techniques have been established for the detection of PFOS, including high-performance liquid chromatography (HPLC), mass spectrometry (MS), and methods that combine them [8,9]. Despite having advantages like high sensitivity and specificity, these approaches are costly, time-intensive, and not conducive to swift on-site detection according to the requirements of versatile application scenarios. In comparison, electrochemical sensing technology has the advantages of being time-saving, rapid, low-cost, having high sensitivity, etc. So it has a promising application for PFOS detection [10]. Recently, metal–organic frameworks (MOFs) and molecularly imprinted polymers (MIPs) have been developed as active sensing materials for electrochemical sensing of PFOS [11].

MOFs, whose inventors won the Nobel Prize in Chemistry in 2025, have attracted special attention due to their extensive uses in many other fields, such as gas storage, catalysis, and pollutant treatment due to their rich pore structure, high specific surface area, adjustable pore size, and abundant porosity [12–14]. When used in electrochemical sensing electrodes, their interface properties can be flexibly regulated by strategies such as metal node doping, ligand functionalization, post-synthesis modification, and defect engineering [15–17]. Compared to other types, Cr-MIL-101 is one of the most typical mesoporous MOFs with an abundant pore structure and good stability, serving as an effective receiving unit upon specific regulation, effectively adsorbing PFOS anions by electrostatic interactions, coordination by Cr metal nodes, anion-π stacking, and hydrophobic hydration. This is because the pore structure of Cr-MIL-101 mainly consists of two types of mesoporous cages between 29 and 34 Å, which are interconnected through pentagonal pore channels (11.7 Å) and hexagonal pore channels (16 Å) [18,19]. Such an architecture could help enhance the adsorption of the analyte molecules and is quite suitable for electrochemical electrode construction for PFOS sensing.

However, MOFs, including Cr-MIL-101, face challenges related to their limited selectivity when utilized in electrochemical sensors. The introduction of functional guests (such as nanomaterials, conducting polymers, and so on) into their channels can significantly improve sensing performances [20,21]. Among these modifiers, MIPs are polymer materials possessing specific molecular recognition capabilities, characterized by high selectivity and stability [22]. Pierpaoli et al. [23] utilized PFOS as a template to create a poly-o-phenylenediamine MIP (PoPD/MIP) for constructing an electrochemical sensor with dual signal response towards PFOS, achieving a limit of detection (LOD) of 1.2 μg/L. However, due to the lack of effective support of the rigid skeleton, the molecularly imprinted cavity of MIPs is prone to deformation or collapse. Moreover, the flexible skeleton of MIPs is easy to aggregate to form dense clusters. These structural deficiencies collectively contribute to reduced adsorption affinity and selectivity, as well as diminished mechanical stability in MIPs [24]. In order to overcome the above limitations, using MOFs as the precursor, researchers loaded MIPs onto the rigid skeleton of MOFs to prepare a MOFs@MIPs composite material with a core–shell structure [25–27]. They combined the porous structure of

MOFs with the high selectivity of MIPs, synergistically enhancing the strength and number of recognition sites, thereby significantly improving the PFOS sensing performance [27,28].

Therefore, in this study, a conducting polymer, poly(3,4-ethylenedioxythiophene) (PEDOT), was selected as a guest to load on Cr-MIL-101 by a molecular imprinting process to construct core–shell Cr-MIL-101@PEDOT/MIP composites (Scheme 1). They can fully integrate the mesoporous characteristics of Cr-MIL-101 and the specific recognition cavity advantages of PEDOT/MIP, showing satisfactory stability and selectivity. They were modified on the surface of a glassy carbon electrode (GCE) to realize the high-performance detection of PFOS under the redox probe strategy. In the quantitative analysis, based on the Freundlich–Langmuir and Langmuir adsorption models, the current signal change was converted into a PFOS concentration, and the LOD was as low as 12.5 ng/L (0.025 nM), which met the limit requirements of PFOS in drinking water in China (80 ng/L) and according to the US EPA (70 ng/L). In addition, Cr-MIL-101@PEDOT/MIP/GCE not only showed high selectivity for common anionic and cationic surfactants, but also for PFAS analogs (current response change < 8.0%). The recovery rate of actual water samples is 97.72–106.82%, which confirms its reliable value in practical applications. This work provides a facile technical route for the efficient detection of PFOS in the water environment, and may have broad prospect in the field of pollution monitoring towards other PFASs.



Scheme 1. Schematic representation of Cr-MIL-101@PEDOT/MIP/GCE for electrochemical detection of PFOS.

2. Materials and Methods

2.1. Synthesis of Cr-MIL-101

The synthesis of Cr-MIL-101 was conducted according to a previous study with minor modifications [18,25]. First, 4.1 g of sodium acetate was dissolved in 1 L of deionized water to prepare a 0.05 M aqueous solution. Subsequently, 4.0 g of chromium nitrate nonahydrate ($Cr(NO_3)_3 \cdot 9H_2O$) and 1.7 g of terephthalic acid (BDC) were weighed and dissolved in the aqueous sodium acetate solution (50 mL) prepared above, and followed by 35 min of ultrasound treatment to ensure complete dissolution. Then, the reaction mixture was placed in a Teflon-lined stainless-steel autoclave and heated to 180 °C for 24 h to facilitate the synthesis of Cr-MIL-101 nanoparticles. Subsequently, the autoclave was allowed to

cool to ambient temperature naturally. The light green precipitate (Cr-MIL-101) obtained initially was centrifugally washed twice in deionized water and ethanol, respectively. The solid obtained by centrifugation was dried in an oven at 80 °C for 24 h.

2.2. Synthesis of Cr-MIL-101@PEDOT/MIP

The polymerization of 3,4-ethylenedioxythiophene (EDOT) monomer was carried out in the ammonium persulfate (APS)/hydrochloric acid (HCl) system, which was improved upon from previous studies [29]. EDOT (142.0 mg) was dissolved in 50 mL of ethanol and sonicated for 15 min to render a uniform dispersion. Different quantities of Cr-MIL-101 powder (5.0, 10.0, 20.0, 30.0, 40.0, and 50.0 mg) were dispersed ultrasonically in 15 mL of deionized water. Then 5 mL of the ethanol dispersion of EDOT was stirred with 15 mL of different aqueous dispersions of Cr-MIL-101 for 30 min. Subsequently, 10.0 mL of APS/HCl mixture was added, and the reaction lasted at room temperature for 12 h. The resulting dark blue powder was obtained by removing the supernatant, followed by centrifugation with deionized water and ethanol for three cycles. The material was dried in an oven at 60 °C to yield the template-free composite material (Cr-MIL-101@PEDOT/NIP). The synthesis of Cr-MIL-101@PEDOT/MIP follows a similar preparation protocol to that outlined above with the PFOS as the template.

2.3. Preparation of Cr-MIL-101@PEDOT/MIP/GCE

The bare GCE was polished in suede by using an alumina powder slurry with average particle sizes of 0.03 and 0.01 μm sequentially, followed by ultrasonic cleaning in deionized water and ethanol for 10 min each. Then the bare GCE was dried in a N_2 stream. After cleaning, 4 μL of Cr-MIL-101@PEDOT/MIP composite suspension (2.5 mg/mL) was drop-coated onto polished 1 mm diameter GCE surfaces and dried at 70 °C for 10 min. Subsequently, the surface of Cr-MIL-101@PEDOT/MIP/GCE was rinsed sequentially with deionized water and ethanol, followed by a repeated drying step.

3. Results and Discussion

3.1. Structures and Properties of Cr-MIL-101@PEDOT/MIP

3.1.1. Morphology

The morphology of the Cr-MIL-101@PEDOT/MIP composite was characterized utilizing scanning electron microscopy (SEM) and transmission electron microscopy (TEM). The microcrystalline particles of Cr-MIL-101 (Figure 1A) demonstrate a typical octahedral shape with sizes of around 300–400 nm, showing consistent size distribution. These morphological characteristics are consistent with earlier reports on the crystal structure of Cr-MIL-101 [12]. The original PEDOT exhibits an irregular, dense, compact clump structure due to a lack of support from the porous framework (Figure 1B). After the preparation of core–shell composites with PEDOT and Cr-MIL-101 as precursor cores, both Cr-MIL-101@PEDOT/NIP (Figure 1C) and Cr-MIL-101@PEDOT/MIP (Figure 1D) display octahedral arrangements with core–shell architectures and are similar in size to Cr-MIL-101 (300–400 nm). The texture of Cr-MIL-101@PEDOT/MIP composites might seem more irregular and rougher, possibly due to the existence of molecular imprint voids.

TEM was used to compare microstructural differences between Cr-MIL-101 and Cr-MIL-101@PEDOT/MIP, confirming the successful creation of a core–shell design in the composites. Analysis showed that Cr-MIL-101 crystals displayed a clear morphology and crystal plane structures, consistent in size with SEM results (300–400 nm) (Figure 1E). The PEDOT/MIP shell was evenly applied onto the crystal surface of Cr-MIL-101 in Cr-MIL-101@PEDOT/MIP, preserving the crystal structure of Cr-MIL-101 (Figure 1F).

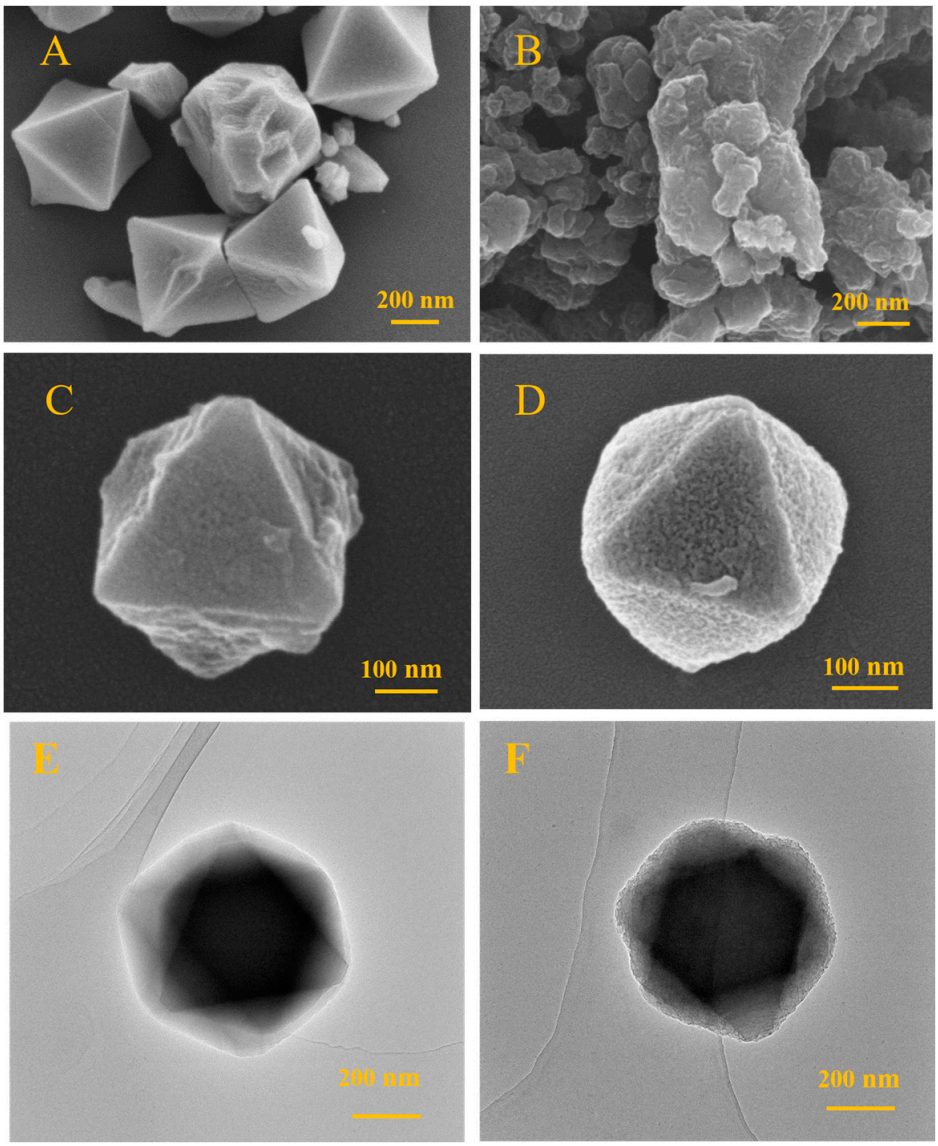


Figure 1. The SEM images of Cr-MIL-101 (**A**), pristine PEDOT (**B**), Cr-MIL-101@PEDOT/NIP (**C**), and Cr-MIL-101@PEDOT/MIP (**D**). The TEM images of Cr-MIL-101 (**E**) and Cr-MIL-101@PEDOT/MIP (**F**).

3.1.2. XRD Analysis

The crystal properties of the Cr-MIL-101 and Cr-MIL-101@PEDOT/MIP were analyzed by X-ray diffraction (XRD). The results are shown in Figure 2A, and the main diffraction characteristic peaks of Cr-MIL-101 at 5.2°, 8.5°, 9.1°, 10.4°, and 16.6° are consistent with the reports in the literature [25,29], while Cr-MIL-101@PEDOT/MIP retains these characteristic peaks well. The reduction in relative peak intensity observed in Cr-MIL-101@PEDOT/MIP can be attributed to the limited infiltration of disordered PEDOT polymer chains into the porous structure of Cr-MIL-101. This infiltration partly impacts the crystal plane diffraction of Cr-MIL-101, consequently leading to a decline in diffraction peak intensity [30,31].

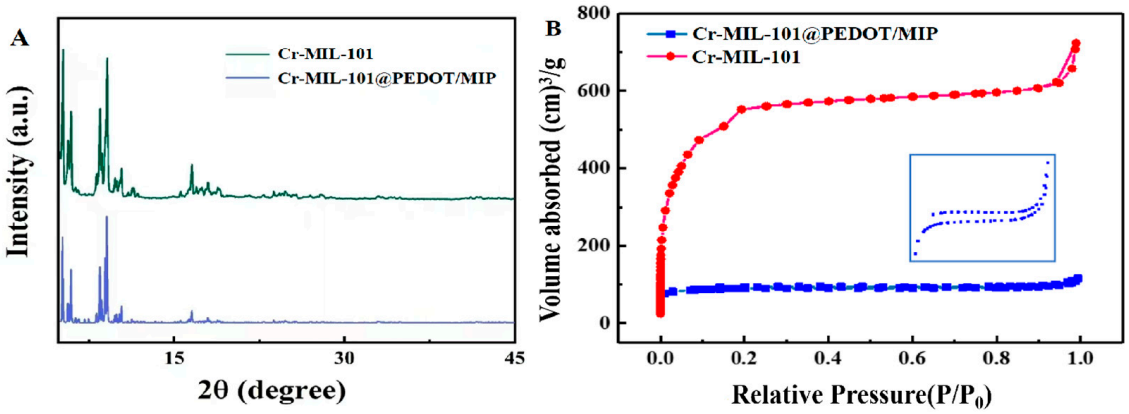


Figure 2. (**A**) The XRD patterns of Cr-MIL-101 and Cr-MIL-101@PEDOT/MIP; (**B**) N_2 adsorption–desorption isotherm of Cr-MIL-101 and Cr-MIL-101@PEDOT/MIP; Insert: Amplification of N_2 adsorption–desorption isotherm for Cr-MIL-101@PEDOT/MIP.

3.1.3. Porous Network Structure Analysis

The effect of the introduction of guest PEDOT/MIP on the pore structure of Cr-MIL-101 was characterized by Brunauer–Emmett–Teller (BET) analysis. Figure 2B presents the N_2 adsorption–desorption isotherms of Cr-MIL-101 and Cr-MIL-101@PEDOT/MIP at 77 K. Cr-MIL-101 shows Type-IV adsorption isotherm characteristics, indicating the presence of a mesoporous pore structure [32]. Before the incorporation of PEDOT/MIP, the synthesized Cr-MIL-101 exhibits a BET specific surface area of 2013.5 m^2/g, a total pore volume of 0.989 cm^3/g, and an average pore size of 2.22 nm. The test results are consistent with the prior literature on Cr-MIL-101 [33], whereas incorporating PEDOT/MIP as a guest resulted in a decrease in the BET surface area to 285.2 m^2/g, a reduction in total pore volume to 0.179 cm^3/g, and an increase in average pore size to 2.51 nm for Cr-MIL-101@PEDOT/MIP. The slight increase in the average pore size distribution is possibly due to PEDOT/MIP blocking the smaller pore structure in Cr-MIL-101 [32]. Moreover, the Cr-MIL-101@PEDOT/MIP composites have an irregular pore structure due to the PEDOT/MIP incorporation, which results in an uneven distribution of adsorption sites. And Cr-MIL-101@PEDOT/MIP composites have different adsorption sites, and each kind of adsorption site shows different adsorption capacities [34]. Therefore, the adsorption and desorption curves of Cr-MIL-101@PEDOT/MIP do not close completely in the low-pressure region.

3.1.4. Surface Chemical Composition Analysis

The surface chemical composition of Cr-MIL-101@PEDOT/MIP was performed by X-ray photoelectron spectroscopy (XPS). The Cr-MIL-101 surface contained C, O, and Cr elements (Figure 3A). In contrast, Cr-MIL-101@PEDOT/MIP also showed S and F elements (Figure 3B). S likely came from PEDOT's thiophene ring and PFOS's sulfonic acid group. F possibly originated from incompletely eluted PFOS's fluorocarbon backbone. The peak intensity of the Cr 2p orbital in Cr-MIL-101@PEDOT/MIP slightly decreases; yet the remarkable binding energy peaks of Cr $2p_{3/2}$ (577.2 eV) and Cr $2p_{1/2}$ (586.4 eV) are observed clearly (Figure 3C) [35]. This indicates that the PEDOT/MIP shell structure does not entirely obstruct the pore structure, allowing some Cr metal nodes to remain exposed on the surface of the Cr-MIL-101@PEDOT/MIP composites [18]. Figure 3D displays the high-resolution spectrum of the S 2p orbital of Cr-MIL-101@PEDOT/MIP. The peaks observed at 163.1 eV and 164.4 eV are linked to the $2p_{3/2}$ and $2p_{1/2}$ orbitals of S within the thiophene of PEDOT, respectively. Moreover, peaks at 167.0 eV and 168.0 eV correspond to the $2p_{3/2}$ and $2p_{1/2}$ orbitals of S within the sulfonic acid group. The electron density undergoes significant changes due to the presence of adjacent O [36]. Previous studies have shown a robust

interaction between Cr metal nodes within Cr-MIL-101 and PFOS sulfonic acid groups [37]. Consequently, it is difficult to completely elute the PFOS template partially adsorbed on the Cr metal nodes of Cr-MIL-101, resulting in the peak for F and the sulfonic acid group. The Cr-MIL-101@PEDOT/MIP composite is consistent with the Raman spectrum of PEDOT, which also indicates the shell–core structure formation [38,39] (Figure S1).

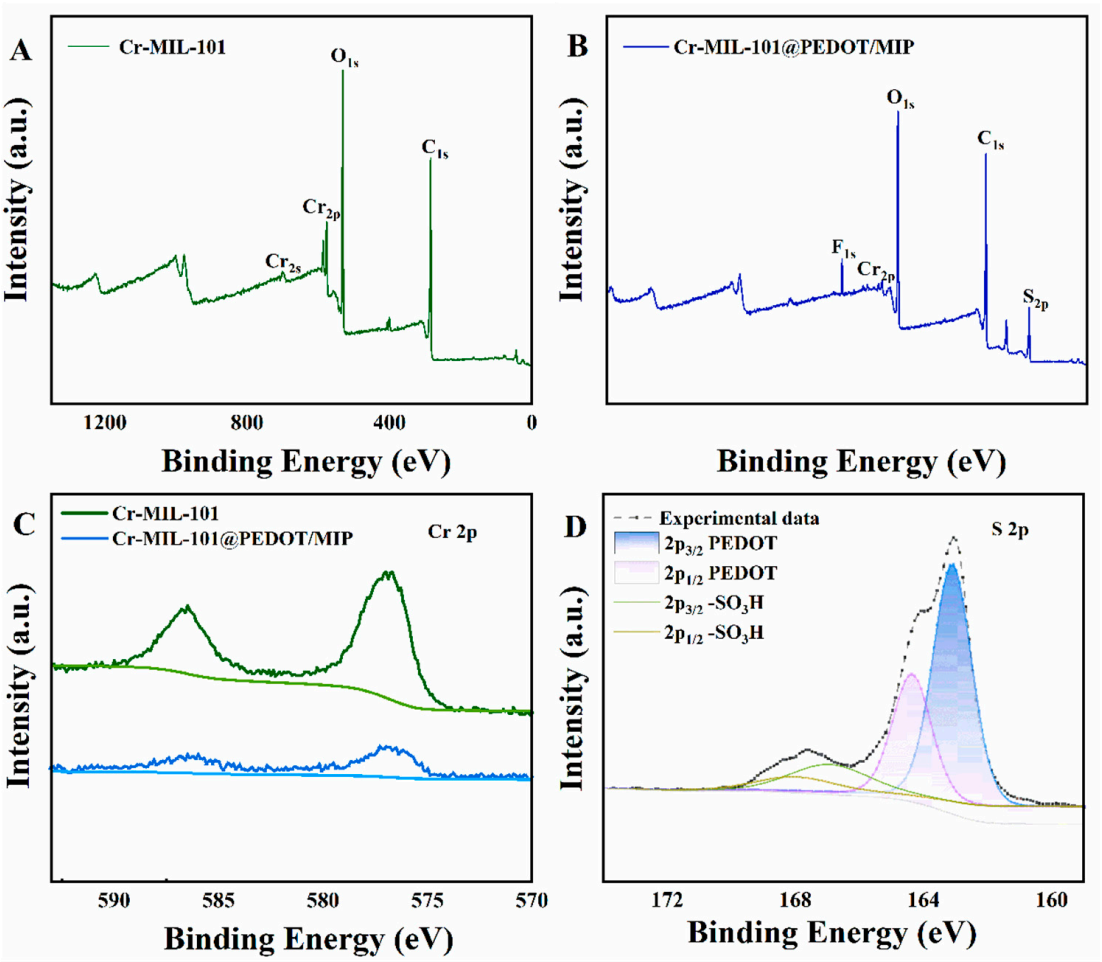


Figure 3. The XPS survey spectra of Cr-MIL-101 (**A**) and Cr-MIL-101@PEDOT/MIP (**B**); the XPS high-resolution spectra of Cr 2p for Cr-MIL-101 and Cr-MIL-101@PEDOT/MIP (**C**); the XPS high-resolution spectra of S 2p for Cr-MIL-101@PEDOT/MIP (**D**).

3.2. Electrochemical Detection Performances of PFOS by Cr-MIL-101@PEDOT/MIP/GCE

3.2.1. Electrochemical Impedance Spectroscopy (EIS)

The electrochemical impedance spectroscopy (EIS) data for the bare GCE, Cr-MIL-101/GCE, and Cr-MIL-101@PEDOT/MIP/GCE are presented in the format of Nyquist plots (Figure 4). The bare GCE exhibits the largest semi-circular region in the high-frequency range, indicating that charge transfer impedance (Rct) is larger. The Rct of Cr-MIL-101/GCE decreases slightly, whereas that of Cr-MIL-101@PEDOT/MIP/GCE decreases significantly. This result evinces an enhancement in the conducting properties of the core–shell composites after the introduction of PEDOT/MIP. The Cr-MIL-101@PEDOT/MIP/GCE has enhanced electrochemical signal response capabilities. And the Cr-MIL-101@PEDOT/MIP/GCE also has the largest electrochemical active areas [40] (Figure S2).

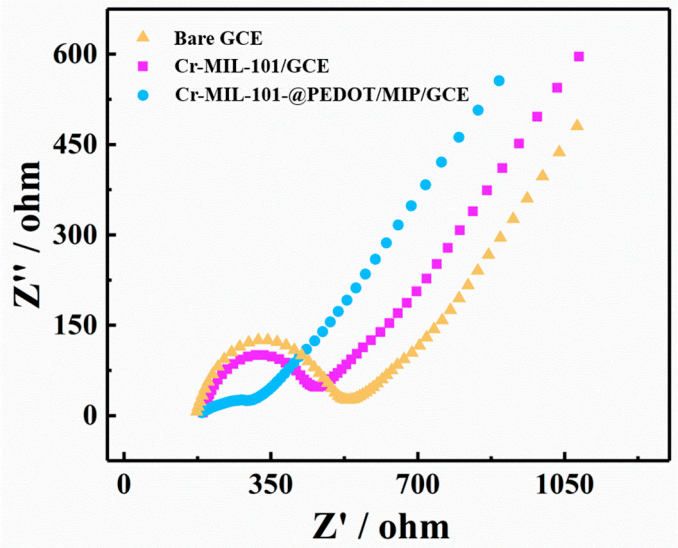


Figure 4. The Nyquist plots measured by EIS of bare GCE, Cr-MIL-101/GCE, and Cr-MIL-101@PEDOT/MIP/GCE.

3.2.2. Quantitative Detection

The differential pulse voltammetry (DPV) method was employed to quantitatively detect the PFOS concentrations by the redox probe strategy. As shown in Figure 5A, the oxidation peak currents of the redox probe decrease with the addition of PFOS over a concentration range of 0.1–200 nM. The Langmuir model and Freundlich–Langmuir model were used for PFOS quantitative analysis. The detection mechanism was described in the Supplementary Materials [41]. Fitting those isotherm models to the electrochemical experimental data can effectively analyze PFOS concentrations. As shown in Figure 5B, the hybrid Freundlich–Langmuir model can effectively fit the experimental data over a wide concentration range (R^2 = 0.982). The corresponding K_A value is 1.247 ± 0.047 nM^{-1}, and the m value is 0.606 ± 0.016.

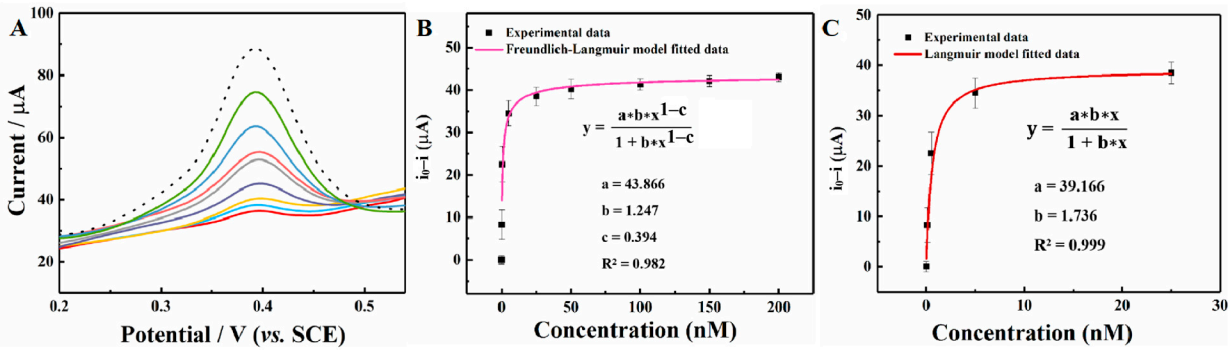


Figure 5. (**A**) The DPV responses of a redox probe in the presence of 0.1, 0.5, 5, 25, 50, 100, 150, and 200 nM of PFOS (dotted line: no PFOS addition; scan rate: 50 mV/s); (**B**) the decrease in peak current as a function of the PFOS concentrations (0.1–200 nM) fitted with the Freundlich–Langmuir model; (**C**) the decrease in peak current as a function of the PFOS concentrations (0.1–25.0 nM) fitted with the Langmuir model; error bar (n = 3).

However, the redox probe decreasing value is better described by the Langmuir adsorption isotherm model at low concentrations, indicating a highly homogeneous interface with a heterogeneity parameter m of 1. As shown in Figure 5C, the redox probe decreasing value of low PFOS concentrations (0.1–25.0 nM) was analyzed with the Langmuir isotherm adsorption model (R^2 = 0.999). And a larger K_A value (1.736 ± 0.032 nM^{-1})

was obtained, suggesting a better affinity of the initial adsorption process. This result is probably caused by PFOS molecules that tend to interact with active sites with a high adsorption affinity. Compared to the template-free Cr-MIL-101@PEDOT/NIP/GCE, the Cr-MIL-101@PEDOT/MIP/GCE can effectively recognize PFOS molecules and cause the redox probe current decrease in low concentrations (Figure S3). Furthermore, Figure S4 shows the simulation for the optimal adsorption site of the PFOS molecule on the Cr-MIL-101 and PEDOT. PFOS molecules may first preempt a single type of active adsorption site with high affinity on the Cr-MIL-101@PEDOT/MIP/GCE interface. Therefore, utilizing the Langmuir adsorption isotherm model, the LOD can be estimated as 0.025 nM with the definition of three times the background signal standard deviation. A comparison of previous studies on electrochemical detection of PFOS and this work is shown in Table 1. The result reveals that Cr-MIL-101@PEDOT/MIP/GCE exhibits a low LOD and demonstrates promising analytical capabilities for detecting trace amounts of PFOS.

Table 1. The results from comparison of this work with previously reported electrochemical detection methods towards PFOS.

Detection Mechanism	Modified Electrode	Linear Range	LOD	Ref.
PFOS inhibiting EBC caused open-circuit potential decreasing	GLDH/MWNHs/GCE	5–500 nM	1.6 nM	[42]
PFOS/MB ion-pair caused potential increasing	PPy/MIP/PLE	10 μM–10 mM	100 nM	[43]
PFOS blocking caused probe charge-transfer resistance increasing	MIP/PoPD/GCME	0.05–0.5 nM	3.4 pM	[10]
PFOS blocking caused probe current decreasing	MIPPDA/AuNPs/GCE	0.01–8 μM	4.2 nM	[44]
	MIP/PoPD/GCME	0.05–0.5 nM; 1–500 nM	0.05 nM	[45]
	Cr-MIL-101@PEDOT/MIP/GCE	0.1–200 nM	0.025 nM	This work

Abbreviations: Enzymatic biofuel cell (EBC); glutamic dehydrogenase combined multi-walled carbon nanohorns modified glassy carbon electrode (GLDH/MWNHs/GCE); methylene blue (MB); molecular imprinting polypyrrole modified pencil lead electrode (PPy/MIP/PLE); molecular imprinting o-phenylenediamine modified glassy carbon microelectrode (MIP/PoPD/GCME); molecular imprinting polydopamine composites with Au nanoparticle modified glassy carbon electrode (MIPPDA/AuNPs/GCE).

3.2.3. Reproducibility, Stability, and Selectivity

In the presence of 25 nM of PFOS, the peak current attenuation signal response of the redox probe of Cr-MIL-101@PEDOT/MIP/GCE from six batches exhibited a variation of less than 6.00%, with relative a standard deviation (RSD) ranging from 1.09% to 1.67% (Figure S5). This finding underscores the satisfactory reproducibility of Cr-MIL-101@PEDOT/MIP/GCE. The Cr-MIL-101@PEDOT/MIP/GCE underwent storage at room temperature and assessment on the 14th day. The corresponding redox probe peak current decay signal only decreased to 97.20% of the initial value, exhibiting the RSD of 1.51–2.93% (Figure S6). These outcomes suggest the long-term stability of the Cr-MIL-101@PEDOT/MIP composites. Moreover, the study investigated the interference resistance of Cr-MIL-101@PEDOT/MIP/GCE against 1 mM of common inorganic salt anions (K^+, Na^+, NO_3^-, HCO_3^-, Cl^-), 25 nM of common surfactants (sodium dodecyl sulfate, SDS; cetyltrimethylammonium bromide, CTAB), and typical short-chain PFASs (perfluorobutyric acid, PFBA; perfluorobutanesulfonic acid, PFBS) and long-chain PFASs (perfluorooctanoic, PFOA; perfluorodecanoic acid, PFDA). After subtracting the signal measured in the presence of interferents from the signal measured in the absence of interferents, the current signal changes in ions and surfactants were all less than ±5% (Figure S7). It is satisfactory

that Cr-MIL-101@PEDOT/MIP/GCE demonstrated robust anti-interference capabilities during the selectivity assessment of other PFAS family analogs. The variation in peak current response signal of the redox probe was less than 8%, underscoring the satisfactory selectivity of Cr-MIL-101@PEDOT/MIP/GCE.

3.2.4. Real Sample Detection

The real sample detection performance of Cr-MIL-101@EDOT/MIP/GCE was evaluated by detecting PFOS in tap water, Wei River water, and campus lake water samples with a standard addition method. The results are shown in Table 2. The recovery ranges for them under three PFOS concentration levels are 104.71–118.42%, 94.98–112.27%, and 105.50–117.76%, respectively. The above experimental results demonstrate that Cr-MIL-101@PEDOT/MIP/GCE exhibits strong resistance to interference in complex matrix water samples. This indicates its promising potential for efficient and rapid monitoring of PFOS in real environmental water samples.

Table 2. The recoveries of Cr-MIL-101@PEDOT/MIP/GCE for real-environment sample detection.

Samples	Spiked (nM)	Measured (nM)	Recovery (%)	RSD (%) (n = 3)
Tap water	0	-	-	-
	1.00	0.9871	98.71	3.13
	10.00	10.332	103.32	4.81
	100.00	103.11	103.11	3.83
Wei River water	0	-	-	-
	1.00	1.0682	106.82	4.55
	10.00	10.493	104.93	3.42
	100.00	97.72	97.72	4.37
Campus lake water	0	-	-	-
	1.00	1.0671	106.71	3.69
	10.00	10.503	105.03	2.37
	100.00	98.50	98.50	4.91

The real-environment samples were obtained from Shaanxi, China. All the water sample (1 L) was mixed with ethylenediaminetetraacetic acid disodium salt (EDTA) (1 g) and filtered with 0.22 μm fiberglass paper. The Wei River water was collected at the latitude of 34.467653, and the longitude of 109.103633. The campus lake water was collected at Shaanxi University of Science and Technology, latitude 34.327084, longitude 108.915300.

4. Conclusions and Outlook

In this study, Cr-MIL-101@PEDOT/MIP/GCE was constructed by the host–guest preparation strategy using a Cr-MIL-101 precursor and PEDOT/MIP shell, achieving highly selective and sensitive detection of PFOS. In Cr-MIL-101, Cr cation nodes efficiently capture PFOS anions through electrostatic interactions, coordination, and hydrophobic hydration. And PEDOT/MIP offers specific recognition sites and enhances electron transport. The Cr-MIL-101@PEDOT/MIP composites address the constraints associated with individual MOFs and MIPs. The Cr-MIL-101@PEDOT/MIP/GCE not only has a wide detection range (0.1–200 nM) and a low LOD (0.025 nM) for PFOS, but it also has immunity to interference with other members within PFASs and other contaminants (the current response signal does not change more than 8.0%). The real sample detection demonstrates the recovery ranging from 97.72% to 106.82%, confirming the reliability of Cr-MIL-101@PEDOT/MIP/GCE in real environmental sample detection. This study not only introduces a novel and effective sensing platform for detecting trace levels of PFOS but also offers insights for developing multiple collaborative functional sensing interfaces, thereby holding significant practical implications in environmental monitoring.

Supplementary Materials: The following supporting information can be downloaded at https://www.mdpi.com/article/10.3390/chemosensors13110378/s1, Details of materials and instruments; structural characterization of the Cr-MIL-101@PEDOT/MIP composite; electrochemical behavior and active surface area of the Cr-MIL-101@PEDOT/MIP/GCE; detection mechanism and theoretical calculations of PFOS on the composite interfaces; reproducibility, stability, and selectivity of the sensors.

Author Contributions: Conceptualization, J.L. and H.M.; Methodology, J.L. and H.M.; Software, Y.M.; Validation, J.L. and H.M.; Formal analysis, Y.M., J.L. and H.M.; Investigation, Q.T.; Resources, Q.T.; Data curation, Y.M.; Writing—original draft preparation, J.L. and H.M.; Writing—review and editing, S.C., Q.T., B.L., C.W. and H.D.; Visualization, Q.T.; Supervision, S.C., Q.T., B.L., C.W. and H.D.; Project administration, S.C.; Funding acquisition, Q.T. and H.D. All authors have read and agreed to the published version of the manuscript.

Funding: This research was funded by [the National Natural Science Foundation of China], grant number [82560770]; [the Tian Chi Talent Innovation Project], grant number [2025CXLJ003] and [the Research Initiation Project for High-level Talents of Yili Normal University], grant number [2505RCYJ03].

Institutional Review Board Statement: Not applicable.

Informed Consent Statement: Not applicable.

Data Availability Statement: The date support that the findings of this study are available on request from the corresponding author.

Acknowledgments: The authors express profound gratitude to Yili Normal University for its innovative training program (X202510764003).

Conflicts of Interest: The authors declare no conflicts of interest.

References

1. Arias Espana, V.A.; Mallavarapu, M.; Naidu, R. Treatment technologies for aqueous perfluorooctanesulfonate (PFOS) and perfluorooctanoate (PFOA): A critical review with an emphasis on field testing. *Environ. Technol. Innov.* **2015**, *4*, 168–181. [CrossRef]
2. Radetić, L.; Plantak, L.; Loborec, J.; Grčić, I. Super-resistance of PFOS in water: Is it beatable? *Chemosphere* **2024**, *362*, 142922. [CrossRef]
3. Mao, W.; Li, M.; Xue, X.Y.; Cao, W.; Wang, X.F.; Xu, F.L.; Jiang, W. Bioaccumulation and toxicity of perfluorooctanoic acid and perfluorooctane sulfonate in marine algae *Chlorella* sp. *Sci. Total Environ.* **2023**, *870*, 161882. [CrossRef] [PubMed]
4. Vierke, L.; Berger, U.; Cousins, I.T. Estimation of the acid dissociation constant of perfluoroalkyl carboxylic acids through an experimental investigation of their water-to-air transport. *Environ. Sci. Technol.* **2013**, *47*, 11032–11039. [CrossRef]
5. Sungur, Ş. Dietary exposure to perfluorooctanoic acid (PFOA) and perfluorooctane sulfonic acid (PFOS): A review of recent literature. *Toxin Rev.* **2017**, *37*, 106–116. [CrossRef]
6. Nguyen, G.T.H.; Nocentini, A.; Angeli, A.; Gratteri, P.; Supuran, C.T.; Donald, W.A. Perfluoroalkyl substances of significant environmental concern can strongly inhibit human carbonic anhydrase isozymes. *Anal. Chem.* **2020**, *92*, 4614–4622. [CrossRef]
7. van der Veen, I.; Fiedler, H.; de Boer, J. Assessment of the per- and polyfluoroalkyl substances analysis under the Stockholm Convention—2018/2019. *Chemosphere* **2022**, *313*, 137549. [CrossRef] [PubMed]
8. Heo, D.-G.; Lee, D.-C.; Kwon, Y.-M.; Seol, M.-J.; Moon, J.S.; Chung, S.M.; Kim, J.-H. Simultaneous determination of perfluorooctanoic acid and perfluorooctanesulfonic acid in Korean sera using LC-MS/MS. *J. Chromatogr. B* **2022**, *1192*, 123138. [CrossRef]
9. Inoue, K.; Okada, F.; Ito, R.; Kawaguchi, M.; Okanouchi, N.; Nakazawa, H. Determination of perfluorooctane sulfonate, perfluorooctanoate and perfluorooctane sulfonylamide in human plasma by column-switching liquid chromatography-electrospray mass spectrometry coupled with solid-phase extraction. *J. Chromatogr. B* **2004**, *810*, 49–56. [CrossRef]
10. Clark, R.B.; Dick, J.E. Electrochemical sensing of perfluorooctanesulfonate (PFOS) using ambient oxygen in river water. *ACS Sens.* **2020**, *5*, 3591–3598. [CrossRef]
11. Liu, T.; Sun, B.; Sang, C.Y.; Cai, H.; Liu, H.; Liu, Y.W.; He, G.S. Rapid detection of perfluorodecanoic acid and perfluorooctanesulfonic acid in foods using a molecularly imprinted poly(o-phenylenediamine)/modified glassy carbon electrode. *J. Agric. Food Chem.* **2025**, *73*, 8073–8083. [CrossRef]

12. Zhao, C.W.; Xu, Y.; Xiao, F.; Ma, J.; Zou, Y.B.; Tang, W.J. Perfluorooctane sulfonate removal by metal-organic frameworks (MOFs): Insights into the effect and mechanism of metal nodes and organic ligands. *Chem. Eng. J.* **2021**, *406*, 126852. [CrossRef]
13. Ruan, X.F.; Liu, D.; Niu, X.H.; Wang, Y.J.; Simpson, C.D.; Cheng, N.; Du, D.; Lin, Y.H. 2D graphene oxide/Fe-MOF nanozyme nest with superior peroxidase-like activity and its application for detection of woodsmoke exposure biomarker. *Anal. Chem.* **2019**, *91*, 13847–13854. [CrossRef] [PubMed]
14. Zhang, Y.P.; Zheng, X.J.; Guo, X.M.; Zhang, J.H.; Yuan, A.H.; Du, Y.K.; Gao, F. Design of modified MOFs electrocatalysts for water splitting: High current density operation and long-term stability. *Appl. Catal. B-Environ.* **2023**, *336*, 122891. [CrossRef]
15. Karbassiyazdi, E.; Kasula, M.; Modak, S.; Pala, J.; Kalantari, M.; Altaee, A.; Esfahani, M.R.; Razmjou, A. A juxtaposed review on adsorptive removal of PFAS by metal-organic frameworks (MOFs) with carbon-based materials, ion exchange resins, and polymer adsorbents. *Chemosphere* **2023**, *311*, 136933. [CrossRef] [PubMed]
16. Li, K.; Lin, S.L.; Li, Y.S.; Zhuang, Q.X.; Gu, J.L. Aqueous-phase synthesis of mesoporous Zr-based MOFs templated by amphoteric surfactants. *Angew. Chem. Int. Ed.* **2018**, *57*, 3439–3443. [CrossRef]
17. Yu, C.; Bourrelly, S.; Martineau, C.; Saidi, F.; Bloch, E.; Lavrard, H.; Taulelle, F.; Horcajada, P.; Serre, C.; Llewellyn, P.L.; et al. Functionalization of Zr-based MOFs with alkyl and perfluoroalkyl groups: The effect on the water sorption behavior. *Dalton Trans.* **2015**, *44*, 19687–19692. [CrossRef]
18. Cheng, Y.H.; Barpaga, D.; Soltis, J.A.; Shutthanandan, V.; Kargupta, R.; Han, K.S.; McGrail, B.P.; Motkuri, R.K.; Basuray, S.; Chatterjee, S. Metal-organic framework-based microfluidic impedance sensor platform for ultrasensitive detection of perfluorooctanesulfonate. *ACS Appl. Mater. Interfaces* **2020**, *12*, 10503–10514. [CrossRef]
19. Barpaga, D.; Zheng, J.; Han, K.S.; Soltis, J.A.; Shutthanandan, V.; Basuray, S.; McGrail, B.P.; Chatterjee, S.; Motkuri, R.K. Probing the sorption of perfluorooctanesulfonate using mesoporous metal–organic frameworks from aqueous solutions. *Inorg. Chem.* **2019**, *58*, 8339–8346. [CrossRef]
20. Darwish, M.A.; Abd-Elaziem, W.; Elsheikh, A.; Zayed, A.A. Advancements in nanomaterials for nanosensors: A comprehensive review. *Nanoscale Adv.* **2024**, *6*, 4015–4046. [CrossRef]
21. Meer, S.; Kausar, A.; Iqbal, T. Trends in Conducting polymer and hybrids of conducting polymer/carbon nanotube: A review. *Polym.-Plast. Technol. Eng.* **2016**, *55*, 1416–1440. [CrossRef]
22. Basak, S.; Venkatram, R.; Singhal, R.S. Recent advances in the application of molecularly imprinted polymers (MIPs) in food analysis. *Food Control* **2022**, *139*, 109074. [CrossRef]
23. Pierpaoli, M.; Szopińska, M.; Olejnik, A.; Ryl, J.; Fudala-Ksiażek, S.; Łuczkiewicz, A.; Bogdanowicz, R. Engineering boron and nitrogen codoped carbon nanoarchitectures to tailor molecularly imprinted polymers for PFOS determination. *J. Hazard. Mater.* **2023**, *458*, 131873. [CrossRef]
24. Lahcen, A.A.; Surya, S.G.; Beduk, T.; Vijjapu, M.T.; Lamaoui, A.; Durmus, C.; Timur, S.; Shekhah, O.; Mani, V.; Amine, A.; et al. Metal-organic frameworks meet molecularly imprinted polymers: Insights and prospects for sensor applications. *ACS Appl. Mater. Interfaces* **2022**, *14*, 49399–49424. [CrossRef]
25. Hou, P.C.; Xing, G.J.; Han, D.; Zhao, Y.; Zhang, G.; Wang, H.; Zhao, C.; Yu, C.N. MIL-101(Cr)/graphene hybrid aerogel used as a highly effective adsorbent for wastewater purification. *J. Porous Mater.* **2019**, *26*, 1607–1618. [CrossRef]
26. Huang, T.Y.; Kung, C.W.; Liao, Y.T.; Kao, S.Y.; Cheng, M.; Chang, T.H.; Henzie, J.; Alamri, H.R.; Alothman, Z.A.; Yamauchi, Y.; et al. Enhanced charge collection in MOF-525-PEDOT nanotube composites enable highly sensitive biosensing. *Adv. Sci.* **2017**, *4*, 1700261. [CrossRef]
27. Guo, W.J.; Jing, Z.W.; Du, Q.Z. Research progress of metal–organic frameworks-molecularly imprinted polymers for specific recognition. *Microchem. J.* **2023**, *191*, 108908. [CrossRef]
28. Karimian, N.; Stortini, A.M.; Moretto, L.M.; Costantino, C.; Bogialli, S.; Ugo, P. Electrochemosensor for trace analysis of perfluorooctanesulfonate in water based on a molecularly imprinted poly(o-phenylenediamine) polymer. *ACS Sens.* **2018**, *3*, 1291–1298. [CrossRef]
29. Zhou, X.; Huang, W.Y.; Shi, J.; Zhao, Z.X.; Xia, Q.B.; Li, Y.W.; Wang, H.H.; Li, Z. A novel MOF/graphene oxide composite GrO@MIL-101 with high adsorption capacity for acetone. *J. Mater. Chem. A* **2014**, *2*, 4722–4730. [CrossRef]
30. Gan, T.; Li, J.B.; Xu, L.P.; Yao, Y.X.; Liu, Y.M. Construction of a voltammetric sensor based on MIL-101 hollow cages for electrocatalytic oxidation and sensitive determination of nitrofurazone. *J. Electroanal. Chem.* **2019**, *848*, 113287. [CrossRef]
31. Le Ouay, B.; Boudot, M.; Kitao, T.; Yanagida, T.; Kitagawa, S.; Uemura, T. Nanostructuration of PEDOT in porous coordination polymers for tunable porosity and conductivity. *J. Am. Chem. Soc.* **2016**, *138*, 10088–10091. [CrossRef]
32. Mutyala, S.; Jonnalagadda, M.; Mitta, H.; Gundeboyina, R. CO_2 capture and adsorption kinetic study of amine-modified MIL-101 (Cr). *Chem. Eng. Res. Des.* **2019**, *143*, 241–248. [CrossRef]
33. Zhao, K.X.; Li, X.; Cheng, G.H.; Liu, L.; Chen, R.N.; Jiao, Y.; Liu, Y.L.; Zhu, G.F. Rapid and selective removal of bisphenol s from environmental samples by surface-imprinted polymer synthesized based on metal-organic framework MIL-101(Cr). *J. Environ. Chem. Eng.* **2024**, *12*, 113569. [CrossRef]

34. Xue, D.-X.; Cairns, A.J.; Belmabkhout, Y.; Wojtas, L.; Liu, Y.; Alkordi, M.H.; Eddaoudi, M. Tunable rare-earth fcu-MOFs: A platform for systematic enhancement of CO_2 adsorption energetics and uptake. *J. Am. Chem. Soc.* **2013**, *135*, 7660–7667. [CrossRef]
35. Wee, L.H.; Bonino, F.; Lamberti, C.; Bordiga, S.; Martens, J.A. Cr-MIL-101 encapsulated Keggin phosphotungstic acid as active nanomaterial for catalysing the alcoholysis of styrene oxide. *Green Chem.* **2014**, *16*, 1351–1357. [CrossRef]
36. Tian, Q.Y.; Xu, J.K.; Xu, Q.; Duan, X.M.; Jiang, F.X.; Lu, L.M.; Jia, H.Y.; Jia, Y.H.; Li, Y.Y.; Yu, Y.F. A poly(3,4-ethylenedioxythiophene): Poly (styrenesulfonate)-based electrochemical sensor for tert-butylhydroquinone. *Microchim. Acta* **2019**, *186*, 772. [CrossRef] [PubMed]
37. Pala, J.; Le, T.; Kasula, M.; Rabbani Esfahani, M. Systematic investigation of PFOS adsorption from water by metal organic frameworks, activated carbon, metal organic framework@activated carbon, and functionalized metal organic frameworks. *Sep. Purif. Technol.* **2023**, *309*, 123025. [CrossRef]
38. Shao, Q.C.; Zhang, X.B.; Liang, P.; Chen, Q.; Qi, X.H.; Zou, M.Q. Fabrication of magnetic Au/Fe_3O_4/MIL-101(Cr) (AF-MIL) as sensitive surface-enhanced Raman spectroscopy (SERS) platform for trace detection of antibiotics residue. *Appl. Surf. Sci.* **2022**, *596*, 153550. [CrossRef]
39. Pan, Y.N.; Wang, W.; Guo, S.; Jin, S.; Park, E.Y.; Sun, Y.T.; Chen, L.; Jung, Y.M. Charge transfer on the surface-enhanced Raman scattering of Ag/4-MBA/PEDOT: PSS system: Intermolecular hydrogen bonding. *Chemosensors* **2021**, *9*, 111. [CrossRef]
40. Islam, M.M.; Kant, R. Generalization of the Anson equation for fractal and nonfractal rough electrodes. *Electrochim. Acta* **2011**, *56*, 4467–4474. [CrossRef]
41. Tian, Q.Y.; Chen, S.; Shi, M.L.; Gao, T.; Zhang, M.; Liao, C.L.; Li, X.M.; Dong, Q.B.; Wang, C.Y. Fluorine-functionalized MOF modified GCE for highly sensitive electrochemical detection of persistent pollutant perfluorooctanoic acid. *Sens. Actuator B Chem.* **2024**, *404*, 135309. [CrossRef]
42. Zhang, T.T.; Zhao, H.M.; Lei, A.; Quan, X. Electrochemical biosensor for detection of perfluorooctane sulfonate based on inhibition biocatalysis of enzymatic fuel cell. *Electrochemistry* **2014**, *82*, 94–99. [CrossRef]
43. Fang, C.; Chen, Z.L.; Megharaj, M.; Naidu, R. Potentiometric detection of AFFFs based on MIP. *Environ. Technol. Innov.* **2016**, *5*, 52–59. [CrossRef]
44. Gao, Y.M.; Gou, W.L.; Zeng, W.P.; Chen, W.; Jiang, J.L.; Lu, J. Determination of perfluorooctanesulfonic acid in water by polydopamine molecularly imprinted/gold nanoparticles sensor. *Microchem. J.* **2023**, *187*, 108378. [CrossRef]
45. Kazemi, R.; Potts, E.I.; Dick, J.E. Quantifying interferent effects on molecularly imprinted polymer sensors for per- and polyfluoroalkyl substances (PFAS). *Anal. Chem.* **2020**, *92*, 10597–10605. [CrossRef]

Disclaimer/Publisher's Note: The statements, opinions and data contained in all publications are solely those of the individual author(s) and contributor(s) and not of MDPI and/or the editor(s). MDPI and/or the editor(s) disclaim responsibility for any injury to people or property resulting from any ideas, methods, instructions or products referred to in the content.